J Nanopart Res (2019) 21: 79
https://doi.org/10.1007/s11051-019-4518-1

RESEARCH PAPER

Carbon cloth–supported Fe_2O_3 derived from Prussian blue as self-standing anodes for high-performance lithium-ion batteries

Jinxiao Shao · Hu Zhou · Meizhou Zhu · Jianhui Feng · Aihua Yuan

Received: 12 September 2018 / Accepted: 22 March 2019 / Published online: 17 April 2019

Abstract The carbon cloth (CC)–supported Prussian blue (PB) composite was firstly prepared by using CC as the substrate and PB as active material through a solution impregnation method. Then, the Fe_2O_3/CC material was obtained by the subsequent high-temperature calcination of PB/CC. This is the first example of composites based on CC and PB (or PB analogues)-derived metal oxides. The resulting Fe_2O_3/CC composite can be employed directly as binder-free anodes for lithium-ion batteries (LIBs), exhibiting superior electrochemical performances to pure CC and Fe_2O_3. The mass specific capacity of Fe_2O_3/CC was about 395 mA h g^{-1} (an areal capacity of 5.1 mA h cm^{-2}) at 100 mA g^{-1} with almost no decay after 135 discharge/charge cycles. The outstanding lithium storage properties of Fe_2O_3/CC benefit from the synergistic interaction between CC and Fe_2O_3.

Keywords Lithium-ion batteries · Self-standing anodes · Carbon cloth · Prussian blue · Fe_2O_3 · Nanocomposites · Energy storage

Electronic supplementary material The online version of this article (https://doi.org/10.1007/s11051-019-4518-1) contains supplementary material, which is available to authorized users.

J. Shao · H. Zhou (✉) · M. Zhu
School of Material Science and Engineering, Jiangsu University of Science and Technology, Zhenjiang 212003, China
e-mail: zhmiao119@sina.com

J. Feng · A. Yuan
School of Environmental and Chemical Engineering, Jiangsu University of Science and Technology, Zhenjiang 212003, China

A. Yuan (✉)
Marine Equipment and Technology Institute, Jiangsu University of Science and Technology, Zhenjiang 212003, China
e-mail: aihua.yuan@just.edu.cn

Introduction

The development of high-performance lithium-ion batteries (LIBs) is an important topic in the field of energy research (Li et al. 2018). Transition metal oxides as promising anode materials of LIBs have attracted much attention due to their high specific capacities and low cost (Goodenough and Park 2013; Wang et al. 2018a). The calcination of metal-organic frameworks (MOFs) is an effective and facile strategy for the preparation of metal oxides or carbon (Ji et al. 2016; Feng et al. 2018). This can be ascribed to the large specific surface areas and suitable channels of MOFs, which facilitate the transmission of lithium ions during the cycles. Among them, metal oxides derived from Prussian blue (PB) with the formula $FeFe(CN)_6$ or PB analogues (PBAs) were considered to be one of the candidate anodes because of the advantages of low cost and abundant resources as well as environmental friendliness (Catala and Mallah 2017; Nie et al. 2014). However, metal oxides generally have the inherent disadvantages such as poor conductivities and large volume changes during the discharge/charge cycles (Wang et al. 2018b). Therefore, it is necessary to combine metal oxides with the conductive and flexible carbonaceous substrates such as porous carbon (Chen et al. 2016), graphene (Ji et al. 2017; Liao et al. 2018; Shao et al. 2019), and carbon

nanotubes (Huang et al. 2015). As we all know, carbon cloth (CC) has been widely employed as a flexible and conductive substrate to composite with active components, and the resulting composites displayed excellent electrochemical properties (Zhao et al. 2016b).

Based on above considerations, the combination of CC and PB (or PBAs)-derived metal oxides will exhibit excellent lithium storage abilities (Zhang et al. 2015), due to the synergistic effect of CC and metal oxides. On the one hand, CC has good flexibility and high conductivity, which can provide rapid channels for the diffusion and migration of electrons. On the other hand, the large specific surface area will afford abundant sites for the nucleation and growth of active materials, and then PB or PBA particles can be easily and uniformly dispersed on the surface of CC. In the present contribution, PB particles in this contribution were firstly grown on CC by a solution immersion strategy (Scheme 1). Subsequently, the Fe_2O_3/CC composite was obtained after high-temperature calcination of PB/CC precursor. To the best of our knowledge, the composites based on CC and PB (PBAs)-derived metal oxides have not been documented to date. The resulting Fe_2O_3/CC composite was directly employed as self-standing anodes and delivered superior electrochemical performances than pure Fe_2O_3 and CC.

Experimental details

Chemical reagents

All chemicals of analytical grade were purchased from Sigma-Aldrich. CC was treated with the concentrated nitric acid, washed several times with deionized water, and then dried at 60 °C overnight.

Syntheses of PB and Fe_2O_3

PB was synthesized according to the reported procedure with slight modifications (Pramudita et al. 2014). 1.646 g of potassium ferricyanide was dispersed in 50 mL of deionized water to form solution A. Solution B was obtained by adding 1.622 g of ferric chloride in deionized water (100 mL). Solution A was slowly poured into solution B under stirring. After being stirred for several minutes, the resulting mixture was placed in an oven and dried for 6 h. The precipitates were separated by centrifuging, washed with ethanol/water (v/v = 1/1), and finally dried overnight. PB products were further calcined at 350 °C for 6 h in a muffle furnace under an air atmosphere. The red-brown Fe_2O_3 products were obtained when the furnace was cooled naturally to room temperature.

Syntheses of PB/CC and Fe_2O_3/CC composites

The pretreated CC (1 cm × 1 cm) and 2 mL of solution A were firstly placed in a small glass vial. After an immersion of 6 h, 2 mL of solution B was added into the above vial. The PB/CC composite was obtained upon shaking gently the vial for several minutes and further standing for 6 h. The obtained sample was washed several times with deionized water and dried. It can be obviously observed that the color of CC changed to blue, demonstrating the successful loading of PB particles. The Fe_2O_3/CC composite was prepared by the calcination of PB/CC precursor by the same method as pure Fe_2O_3 mentioned above. Based on the thermogravimetric (TG) analysis (Fig. S1), the weight fraction of Fe_2O_3 in the composite is calculated to be 13.00% with a loading density of 1.72 mg cm^{-2}, which is higher than those in reported metal oxide/GF composites (Huang et al. 2017; Lin et al. 2016; Wang et al. 2016). In fact, we have carried out considerable synthesis experiments to study the effect of Fe_2O_3 mass loading on the electrochemical performance. However, it is very difficult to further increase the loading ratio of Fe_2O_3 in the composite, because excessive PB particles will easily off from the CC surface upon increasing the concentration of reactants during the preparation process.

Characterizations

The phase structures of all products were performed on a Shimadzu XRD-6000 X-ray diffractometer (XRD). The Raman analyses were conducted on a HR800 Raman spectroscope. Elemental and valence states were analyzed using a Thermo-VG Scientific ESCALAB 250 X-ray photoelectron spectrometer (XPS). TG analyses were conducted on a Pyris Diamond TGA analyzer at a ramp rate of 5 °C min^{-1} under air atmosphere. Scanning electron microscopy (SEM, ZEISS Merlin Compact) was employed to investigate the microstructures, whereas the energy-dispersive spectrometer (EDS, Oxford X-Max) was used to analyze the compositions of materials.

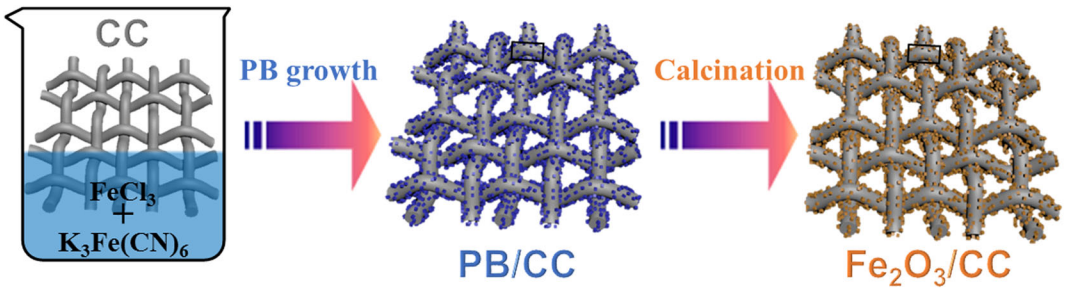

Scheme 1 The preparation process of the Fe_2O_3/CC composite

Electrochemical measurements

The as-prepared CC and Fe_2O_3/CC materials were directly used as self-standing anodes without adding any conductive agent and binder. The mass specific capacity of the composite was based on the total weight of GF and Fe_2O_3, because both components contribute the capacity for the electrode. Accordingly, the areal capacity of the composite is the product of mass specific capacity and weight per area of electrode. For the comparative experiments, pure Fe_2O_3 was mixed with super-P and PVDF with a mass ratio of 7:2:1 in the NMP. The slurry was then coated on copper foil. The battery was assembled and developed using the LAND CT 2001A battery test system. The electrolyte was 1 mol L^{-1} of $LiPF_6$ solution and the test environment was performed at a constant temperature of 25 °C. The materials were subjected to cyclic voltammetry, constant current charge and discharge, and different current multi-rate performance tests. The impedance tests were conducted on an Autolab PGSTAT302N instrument with a test range of 0.01 Hz–100 kHz at an open-circuit voltage.

Results and discussion

As shown in Fig. 1a, the peaks of CC at $2\theta = 26.2°$ and 43.1° corresponded to the (002) and (100) crystal lattice planes of the graphitized carbon. The characteristic peaks of PB were fully consistent with those in the literature (Zhang et al. 2012) and JCPDS card 73-0687, indicating the preparation of the same material. For the PB/CC composite, the diffraction patterns comprised all characteristic peaks of CC and PB, confirming the successful loading of PB particles. The diffraction patterns of Fe_2O_3 obtained by calcining PB precursors were in perfect agreement with the monoclinic phase (JCPDS card 02-1047) (Fig. 1b). In addition, no other peaks were found in the patterns, revealing that PB particles have been completely converted to Fe_2O_3 after the high-temperature treatment. Similarly, the diffraction patterns of Fe_2O_3/CC also contained the characteristic peaks of CC and Fe_2O_3, demonstrating the complete conversion of PB to Fe_2O_3.

SEM images of CC, PB, Fe_2O_3, PB/CC, and Fe_2O_3/CC are displayed in Fig. 2. The CC substrate exhibited a self-standing and flexible structure (Fig. 2a), where carbon fibers formed a dense crossover network by the interconnection way. This type of structure facilitates the nucleation and growth of active materials. The PB particles exhibited a square shape with a side length of about ~ 148 nm (Fig. 2b), typical characteristics of PB (Zhu et al. 2018). The particle surface of PB-derived Fe_2O_3 became rough (Fig. 2c), which can be reasonably attributed to the loss of organic species (C, H) in the framework of PB during the calcination process (Hu et al. 2012). After the loading of PB particles, the color of CC changed from black to blue (Fig. 2d), confirming that the surface of CC was densely wrapped with PB particles. It can be seen from the morphology of PB/CC that PB particles had a similar shape to pure PB. Moreover, these PB particles were densely and uniformly dispersed into the whole network of CC (Fig. 2e, f), which can be ascribed to the large specific surface area of CC and the strong interaction between CC and PB.

The color of CC changed from blue to reddish brown after the calcination of PB/CC precursor (Fig. 2g), confirming that PB particles were completely converted to metal oxides. After a careful observation, the CC substrate still maintained a self-standing structure, and the entire skeleton did not undergo any collapse and destruction after the high-temperature treatment, which can be attributed to the high mechanical strength and flexibility of CC. In addition, Fe_2O_3 particles were also densely loaded on CC and did not

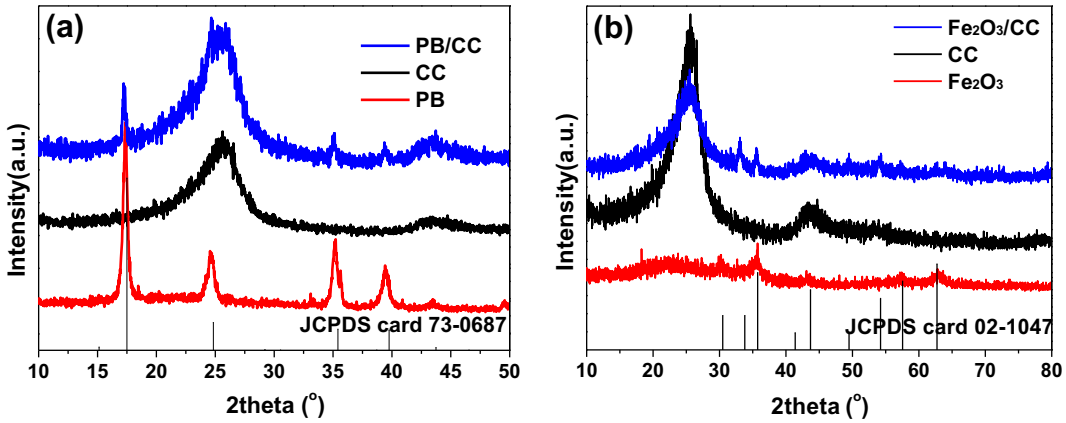

Fig. 1 XRD patterns of the **a** PB/CC and **b** Fe_2O_3/CC systems

fall off from the CC substrate (Fig. 2h). From SEM images of the cross section of Fe_2O_3/CC, the thickness of Fe_2O_3 layer and the diameter of carbon fiber in the composite are 8.37 μm and 0.34 μm, respectively (Fig. S2). Further analysis revealed that the average size and morphology of Fe_2O_3 particles were similar to those of pure Fe_2O_3 (Fig. 2i). Selected area electron diffraction (SAED) pattern (Fig. 2k) indicated the crystallinity of Fe_2O_3 with the rings corresponding to the (440), (400), and (311) planes. High-resolution TEM (HR-TEM) image (Fig. 2l) revealed fringe d-spacings of 0.265 and 0.218 nm, corresponding to the (310) and (321) lattice planes of Fe_2O_3, respectively, in accordance with the result of XRD. According to the elemental mapping distribution, the composite contained the elements of C, O, and Fe. These species were uniformly dispersed into the entire network of CC, further proving the successful loading of Fe_2O_3 (Fig. 2j). The close interaction between Fe_2O_3 particles and the CC substrate plays a crucial role in improving the electrical conductivity and cycle stability of the electrode (Luo et al. 2017).

In the Raman spectrum of PB/CC (Fig. 3a), the Fe–C peaks appeared at 267 cm^{-1} and 532 cm^{-1}, while the C≡N peaks were located at 2093 cm^{-1} and 2151 cm^{-1}. This is consistent with the results reported previously (Jiang et al. 2017). The characteristic peak of CC was also observed, indicating the combination of PB and CC components. The peaks at 200 cm^{-1} and 700 cm^{-1} in the spectra of Fe_2O_3/CC represented the existence of A_{1g} and E_g, respectively, demonstrating the conversion of PB to Fe_2O_3. Similar to PB/CC, the characteristic peak assigned to CC was also observed in the Raman spectrum of Fe_2O_3/CC.

The elemental valence states of Fe_2O_3/CC were investigated by XPS (Fig. 4). The XPS survey spectrum indicated the existence of C, Fe, and O elements. The high-resolution Fe 2p XPS spectrum revealed two strong peaks at 710.9 eV (Fe $2p_{3/2}$) and 724.8 eV (Fe $2p_{1/2}$), which were further decomposed into three peaks of 710.8, 712.5, and 724.8 eV, respectively, indicating the formation of Fe–OH, C–O–Fe, and Fe–O bonds in Fe_2O_3 (Zheng et al. 2018). In addition, both major peaks were accompanied by two weak satellites at 733.1 and 719.2 eV. The O 1s spectrum of the sample exhibited two peaks of 530.1 and 531.6 eV, which are assigned to the O^{2-} forming oxide with iron and OH^-, respectively. The C 1s spectrum revealed the binding energy peaks of 284.5 eV (C–C and C=C) and 285.4 eV (C–O). The XPS results confirmed the successful combination of CC and Fe_2O_3 components.

Figure 5 illustrates CV curves for the first three cycles of CC, Fe_2O_3, and Fe_2O_3/CC electrodes at a sweep speed of 0.2 mV s^{-1} with a voltage window of 0.01 to 3.0 V. It can be found that CV curves of Fe_2O_3/CC contained the characteristic peaks of CC and Fe_2O_3 components. For the composite electrode, a sharp reduction peak at around 0.58 V in the first cathodic scan was ascribed to the conversion reaction between Fe_2O_3 and Li to form Fe and Li_2O, together with the formation of a solid electrolyte interface (SEI) film caused by the decomposition of electrolyte (Zhu et al. 2017). Two broad and weak anodic peaks in the anodic scan at around 1.55 and 1.86 V correspond to the oxidation reaction of Fe and the decomposition of Li_2O to Fe^{3+} (Kobayashi et al. 2018). From the subsequent cycle, this reduction peak potential shifts to a higher voltage of about 0.74 V, indicating the polarization of active

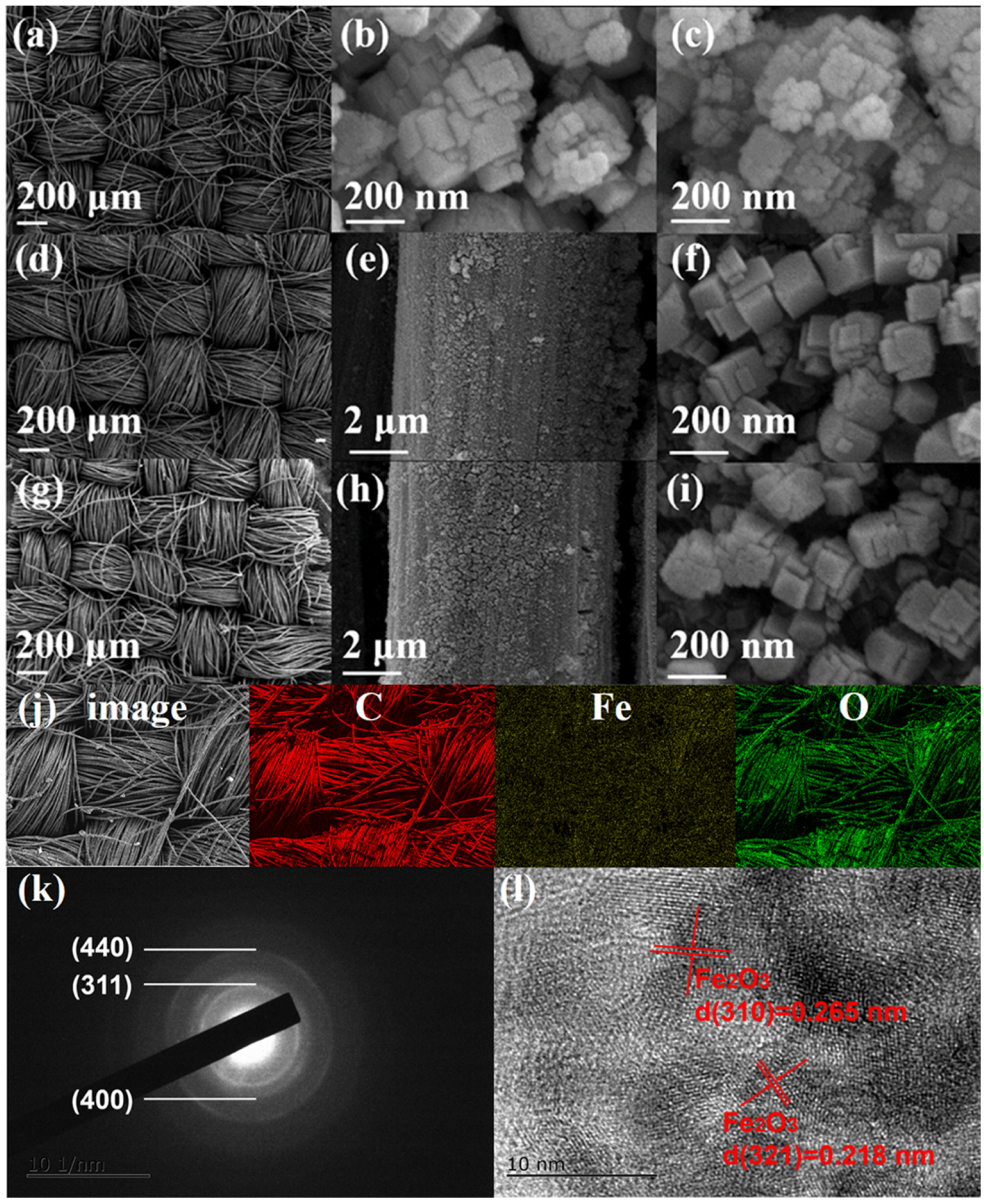

Fig. 2 SEM images of **a** CC, **b** PB, **c** Fe_2O_3, **d**–**f** PB/CC, and **g**–**i** Fe_2O_3/CC; **j** elemental mapping distribution; **k** SAED pattern; and **l** HR-TEM image of Fe_2O_3/CC

material and the existence of irreversible processes during the first cycle. CV curves of the second and third scans overlapped substantially, indicating good redox reversibility and high stability for the composite electrode during the cycles (Zhu et al. 2013).

Figure 6 shows the charge/discharge curves of CC, Fe_2O_3, and Fe_2O_3/CC electrodes at 100 mA g^{-1} in the range of 0.01–3.0 V. The CC substrate exhibited very low capacities (Fig. 6a) of below 90 mA h g^{-1}. For pure Fe_2O_3, the charge and discharge capacities in the first lap were 780 and 1143 mA h g^{-1}, respectively, with the Coulomb efficiency of about 68% (Fig. 6b). The irreversible loss of the initial capacity is due to some irreversible reactions such as the decomposition of electrolyte and the formation of solid electrolyte interphase (SEI) layers (Lv et al. 2017). Subsequent to the 50th lap, the charge/discharge capacity was only 180 and 187 mA h g^{-1}, respectively. For the Fe_2O_3/CC composite, the initial charge/discharge specific capacities were 402 and 544 mA h g^{-1}, respectively, with the

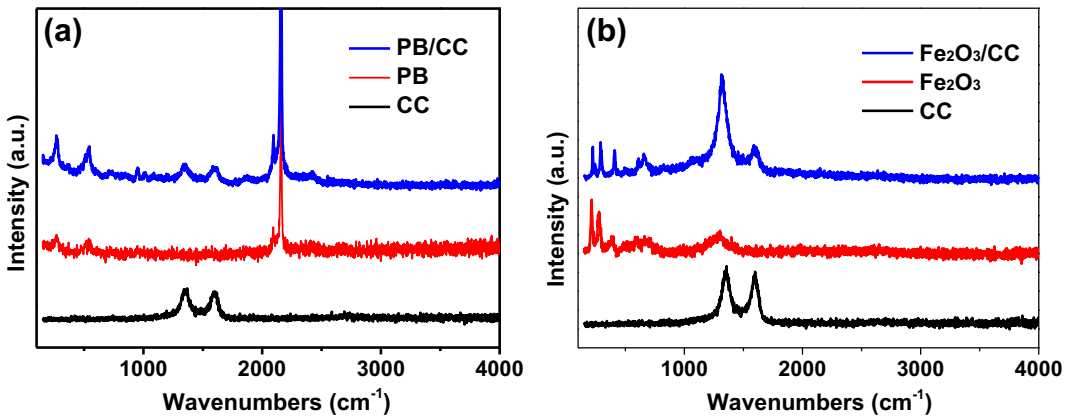

Fig. 3 Raman spectra of the **a** PB/CC and **b** Fe_2O_3/CC systems

Coulomb efficiency of about 74% (Fig. 6b). At the 50th lap, the charge/discharge capacity was 383 and 385 mA h g^{-1}, respectively, with a Coulomb efficiency of 98%. The results showed that the Fe_2O_3/CC composite exhibited a higher charge/discharge efficiency and specific capacity than those observed for pure CC and Fe_2O_3 (Xie et al. 2017).

Figure 7 a shows the cycling performances of CC, Fe_2O_3, and Fe_2O_3/CC at 100 mA g^{-1}. The low specific capacity (~ 63 mA h g^{-1}) for pure CC remained almost unchanged, indicating high cycling stability. For pure Fe_2O_3 electrode, the specific capacity rapidly decayed from the initial 1143 to 81 mA h g^{-1} at 135 cycles with a capacity retention rate of only 7%. The sharp decline in

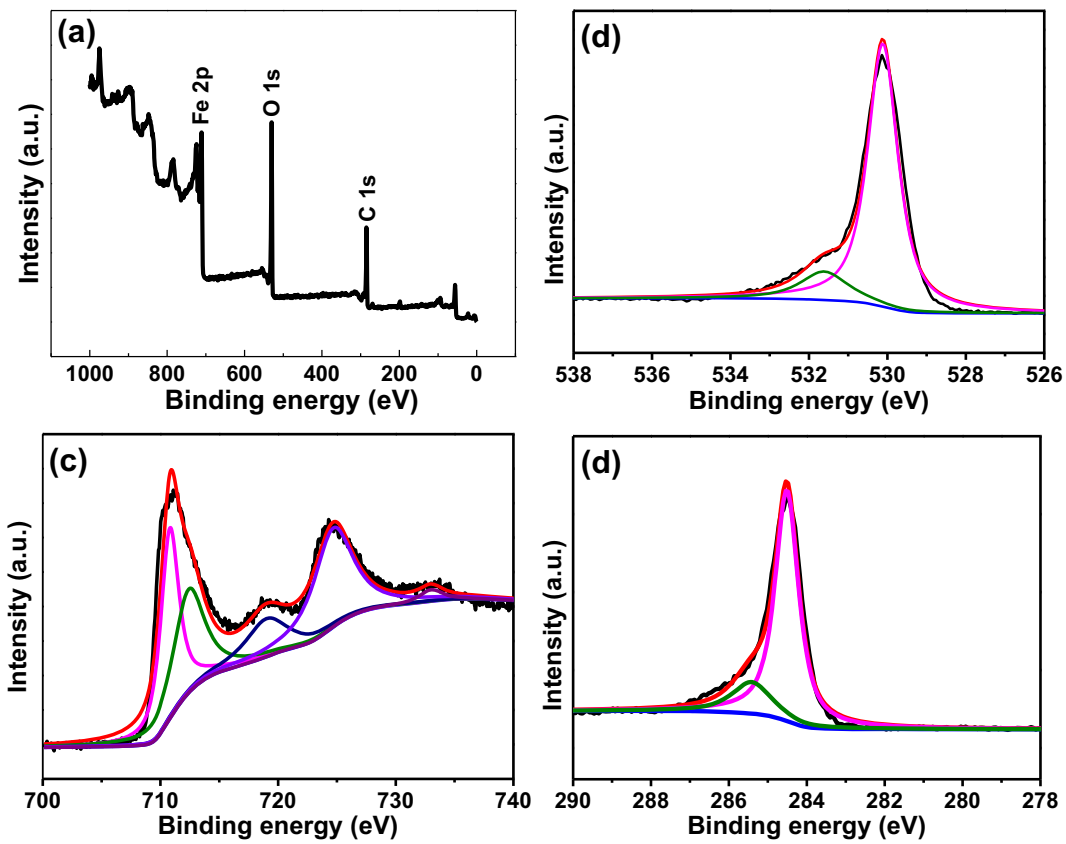

Fig. 4 XPS spectra of the Fe_2O_3/CC composite: **a** survey spectrum, **b** O 1s spectrum, **c** Fe 2p spectrum, and **d** C 1s spectrum

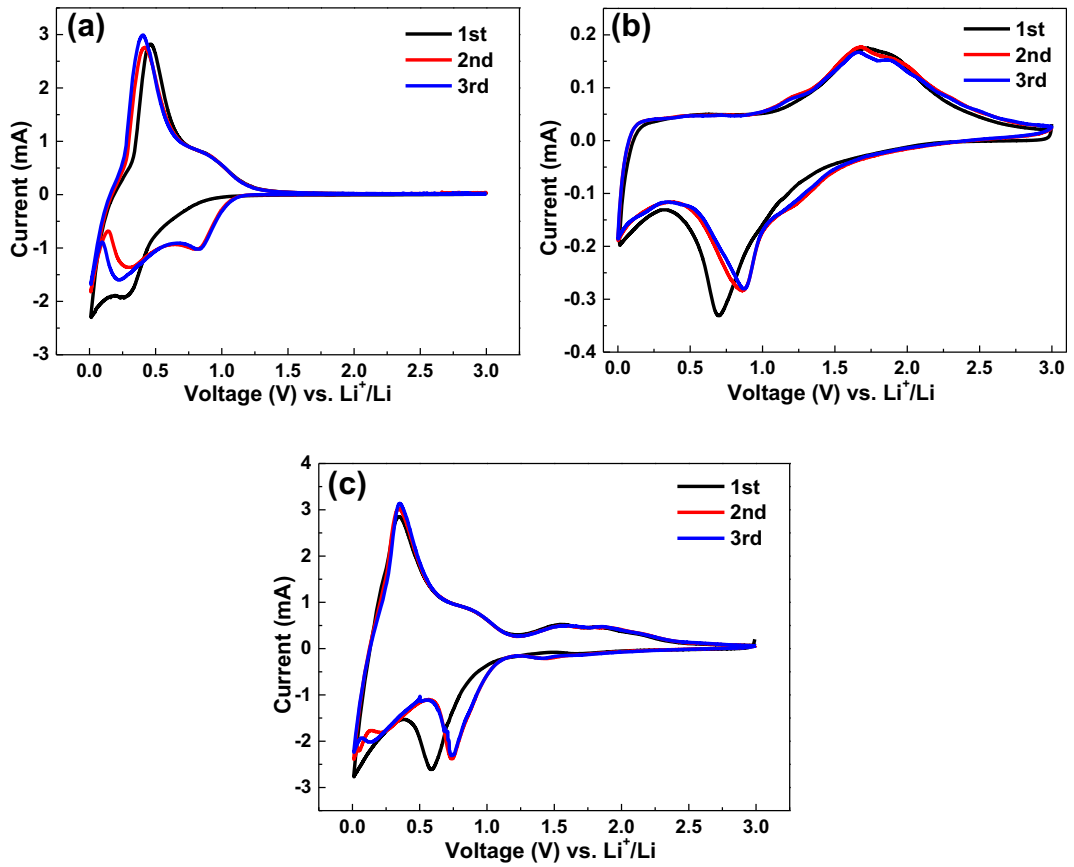

Fig. 5 CV curves of the **a** CC, **b** Fe_2O_3, and **c** CC/Fe_2O_3 electrodes

specific capacity may be ascribed to the significant stacking and structural collapse of Fe_2O_3 particles during the intercalation/delithiation process, as commonly observed in metal oxides (Jiang et al. 2017). In sharp contrast, the capacity of Fe_2O_3/CC remained almost unchanged from the first few laps to the 135th lap, and the capacity at the 135th cycle was still ~ 400 mA h g^{-1}. Notably, the composite delivered a high areal capacity of 5.1 mA h cm^{-2}, while pure Fe_2O_3 only delivered a value of below 0.1 mA h cm^{-2}. In addition, the Coulomb efficiency of the composite was near 100% during the whole cycle process. Based on the above analysis, the composite electrode exhibited a significantly superior cycle performance and capacity retention to pure CC and Fe_2O_3. The significant enhancement in electrochemical performances could be ascribed to the synergistic effect between CC and metal oxide (Zhao et al. 2016a). First, the close combination of Fe_2O_3 nanoparticles with the highly conductive and flexible CC substrate could improve the diffusion kinetics by shortening diffusion pathway for the rapid electron/ion transport. Second, the nanostructured Fe_2O_3 particles could facilitate electrolyte penetration and Li^+ ion diffusion during the cycles. Third, the integrated composite electrode avoids the use of polymer binders and conductive additives, significantly reducing the inactive interface and improving the rate capability. The lithium storage properties of Fe_2O_3/CC can be comparable with those reported Fe_2O_3- or CC-based anode materials as listed in Table 1 (Meng et al. 2017; Kobayashi et al. 2018; Xie et al. 2017; Wei et al. 2015; Tjandra et al. 2016; Cao et al. 2014; Shan et al. 2018; Xu et al. 2017). It is worth mentioning that the areal specific capacities of several graphene-based composites are calculated to be much smaller than our case, although these materials have higher mass specific capacities, which was a common problem associated with lightweight graphene (Ji et al. 2016; Jiang et al. 2017). For example, Fe_2O_3/graphene aerogel displayed a low areal capacity of 0.6 mA h cm^{-2} despite a high mass capacity of 745 mA h g^{-1} at 100 mA g^{-1} after 100 cycles (Meng et al. 2017).

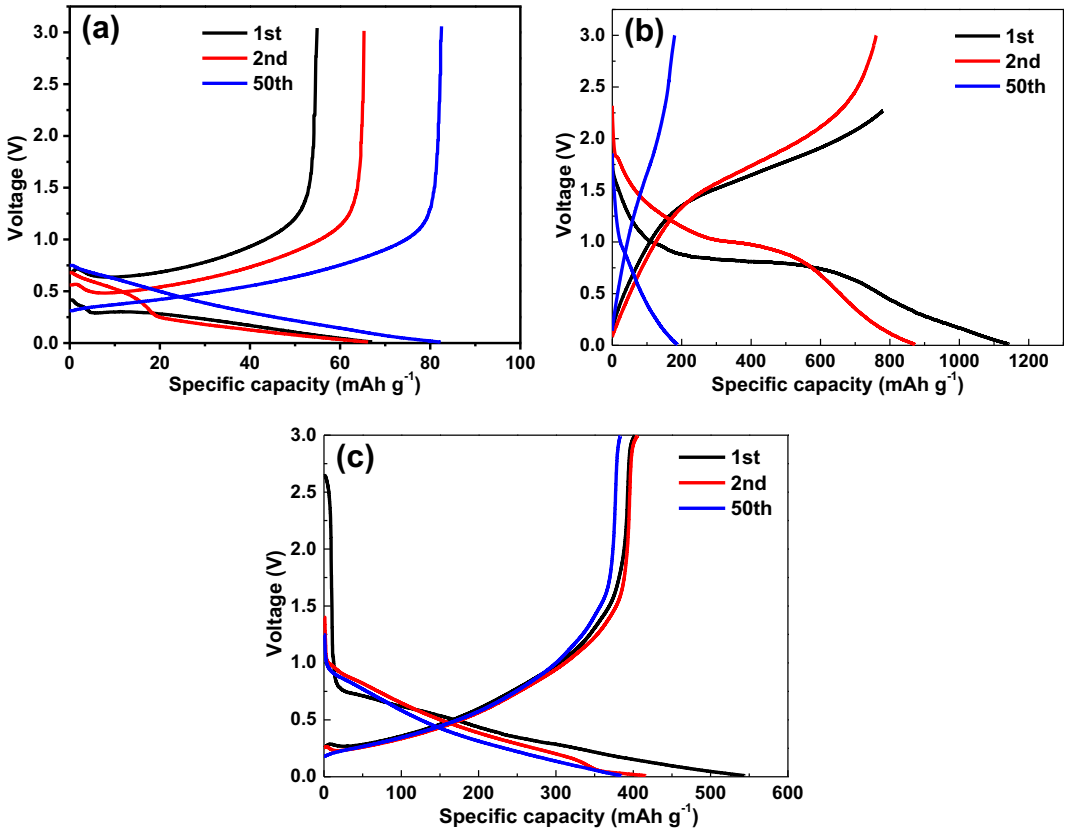

Fig. 6 Charge/discharge curves of the **a** CC, **b** Fe_2O_3, and **c** CC/Fe_2O_3 electrodes at 100 mA g^{-1}

Figure 7 b shows the charge/discharge curves of the CC, Fe_2O_3, and Fe_2O_3/CC electrodes at different current densities. At 20, 50, 100, 200, 500, and 20 mA g^{-1}, the specific capacities of Fe_2O_3/CC were 578, 490, 427, 244, 121, and 557 mA h g^{-1} respectively. The specific capacities of pure Fe_2O_3 decreased significantly, reaching the values of 1425, 541, 315, 99, 22, and 138 mA h g^{-1} at the same current densities, respectively. The CC substrate showed the capacities of 142, 123, 104, 76, 28, and 126 mA h g^{-1} at 20, 50, 100, 200, 500, and 20 mA g^{-1}, respectively. The superior rate capability of Fe_2O_3/CC to pure Fe_2O_3 can be attributed to the high conductivity and flexibility of CC, providing an efficient channel and path for the rapid electron transfer during the electrochemical reaction process (Qiu et al. 2016).

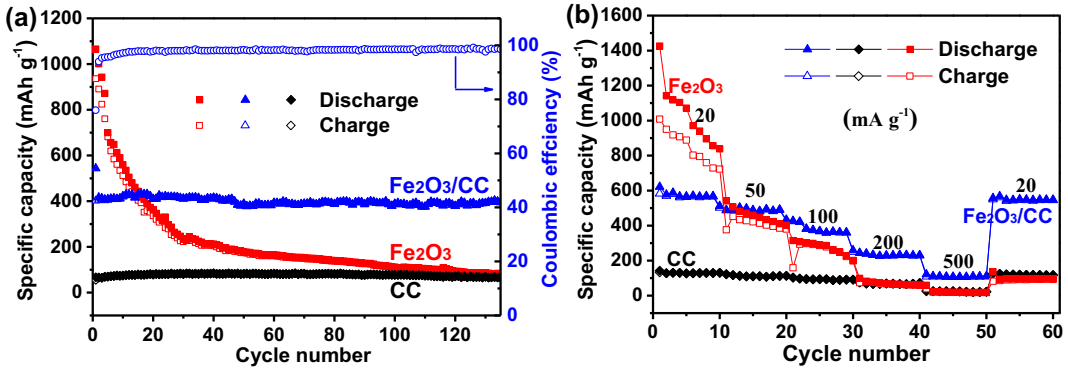

Fig. 7 **a** Cycling performances at 100 mA g^{-1} and **b** the specific capacities at different current densities for the CC, Fe_2O_3, and Fe_2O_3/CC electrodes

Table 1 Comparison of the lithium storage properties of Fe_2O_3/CC with those of reported Fe_2O_3-based or CC-based materials

Electrode materials	Current density	Capacity	Cycles	Refs
Fe_2O_3/CC	100 mA g^{-1} (1.3 mA cm^{-2})	395 mA h g^{-1} (5.1 mA h cm^{-2})	135	This work
Fe_2O_3/graphene aerogel	100 mA g^{-1}	745 mA h g^{-1} (0.6 mA h cm^{-2})	100	Meng et al. 2017
Fe_2O_3/carbon nanofibers	50 mA g^{-1}	518 mA h g^{-1}	100	Kobayashi et al. 2018
Co_3O_4/CC@graphene	100 mA g^{-1}	391 mA h g^{-1}	300	Xie et al. 2017
FeS@C/CC	91 mA g^{-1}	420 mA h g^{-1}	100	Wei et al. 2015
TiO_2/CC	500 mA g^{-1}	150 mA h g^{-1}	100	Tjandra et al. 2016
Fe_2O_3/3D graphene	200 mA g^{-1}	864 mA h g^{-1}	50	Cao et al. 2014
MoS_2@carbon fibers	0.5 mA cm^{-2}	5.3 mA h cm^{-2}	50	Shan et al. 2018
SnO_2/CC	0.2 mA	1.85 mA h cm^{-2}	100	Xu et al. 2017

Figure 8 shows the Nyquist diagrams of Fe_2O_3 and Fe_2O_3/CC before the cycles. The equivalent circuit plot of the material is shown in Fig. 8 (inset), and the fitting values with ZView software of the resistance components in the simplified equivalent circuit are given in Table S1. The depressed semicircle in the high-frequency region presents the charge transfer resistance (R_{ct}), while R_e is the lithium-ion diffusion resistance in the electrolyte. Obviously, the R_e and R_{ct} values of the composite were much smaller than those observed for pure Fe_2O_3. The analysis from EIS indicated that the introduction of CC effectively improved the lithium-ion diffusion and charge transfer process during the Li^+ insertion/extraction reaction, resulting in excellent cycle stability (Xiong et al. 2013). SEM images (Fig. S3) of the Fe_2O_3/CC electrode after the cycles revealed that the composite remained intact free-standing framework. The Fe_2O_3 particles were well preserved and still uniformly coated on the surface of CC except that the particle boundary became smooth. Above result revealed the tight attachment between Fe_2O_3 and CC in the composite during the cycles, which facilitated the enhancement of cycle stability.

Conclusion

In summary, the Fe_2O_3/CC composite was prepared through a solution impregnation method followed by high-temperature calcination. The composite could be used directly as self-standing electrodes for LIBs. Compared with pure CC and Fe_2O_3, the composite exhibited

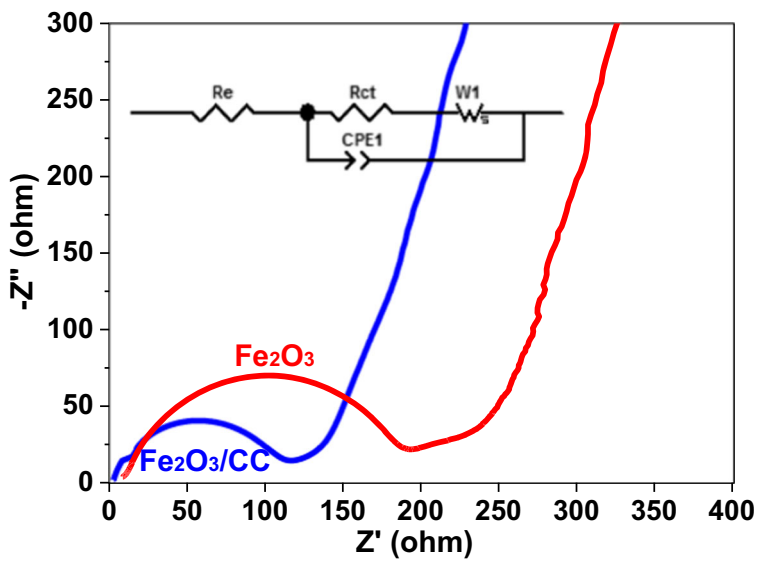

Fig. 8 Nyquist plots of Fe_2O_3 and Fe_2O_3/CC (inset: the simplified equivalent circuit of the electrode material)

a higher mass and areal specific capacity and better cycle stability and rate capability. The outstanding electrochemical properties are ascribed to the synergistic effect between Fe_2O_3 and CC components, where metal oxides contribute a high lithium storage capacity, whereas CC provides excellent conductivity and flexibility. In addition, the close contact between Fe_2O_3 and CC also improves the cycle stability of electrode. This is the first case of composites based on CC and PB (or PB analogues)-derived metal oxides. More importantly, the present research provides some ideas for the design of high-performance integrated electrodes based on the CC substrate.

Funding information This work was financially supported by the National Natural Science Foundation of China (51672114); Natural Science Foundation of Jiangsu Province, China (BK20151328, BK20161357); Foundation from Marine Equipment and Technology Institute for Jiangsu University of Science and Technology, China (HZ20180004); and the project of the Priority Academic Program Development of Jiangsu Higher Education Institutions, China.

Compliance with ethical standards

Conflict of interest The authors declare that they have no competing interest.

References

Cao XH, Zheng B, Rui XH, Shi WH, Yan QY, Zhang H (2014) Metal oxide-coated three-dimensional graphene prepared by the use of metal-organic frameworks as precursors. Angew Chem Int Ed 53:1404–1409

Catala L, Mallah T (2017) Nanoparticles of Prussian blue analogs and related coordination polymers: from information storage to biomedical applications. Coord Chem Rev 346:32–61

Chen T, Hu Y, Cheng BR, Chen RP, Lv HL, Ma LB, Zhu GY, Wang YR, Yan CZ, Tie ZX, Jin Z, Liu J (2016) Multi-yolk-shell copper oxide@carbon octahedra as high-stability anodes for lithium-ion batteries. Nano Energy 20:305–314

Feng JH, Zhou H, Wang JP, Bian T, Shao JX, Yuan AH (2018) MoS_2 supported on MOF-derived carbon with core-shell structure as efficient electrocatalysts for hydrogen evolution reaction. Int J Hydrog Energy 43:20538–20545

Goodenough JB, Park KS (2013) The Li-ion rechargeable battery: a perspective. J Am Chem Soc 135:1167–1176

Hu L, Zhang P, Zhong H, Zheng XR, Yan N, Chen Q (2012) Foamlike porous spinel $Mn_xCo_{3-x}O_4$ material derived from $Mn_3[Co(CN)_6]_2{\cdot}nH_2O$ nanocubes: a highly efficient anode material for lithium batteries. Chem Eur J 18:15049–15056

Huang G, Zhang FF, Du XC, Qin YL, Yin DM, Wang LM (2015) Metal organic frameworks route to in situ insertion of multiwalled carbon nanotubes in Co_3O_4 polyhedra as anode materials for lithium-ion batteries. ACS Nano 9:1592–1599

Huang LY, Wang X, Yin FX, Zhang CW, Gao JW, Liu JM, Zhou GF, Zhang YG, Bakenov Z (2017) Three-dimensional carbon cloth-supported ZnO nanorod arrays as a binder-free anode for lithium-ion batteries. J Nanopart Res 19:42

Ji D, Zhou H, Zhang J, Dan YY, Yang HX, Yuan AH (2016) Facile synthesis of metal-organic framework-derived Mn_2O_3 nanowires coated three-dimensional graphene network for high-performance free-standing supercapacitor electrodes. J Mater Chem A 4:8283–8290

Ji D, Zhou H, Tong YL, Wang JP, Zhu MZ, Chen TH, Yuan AH (2017) Facile fabrication of MOF-derived octahedral CuO wrapped 3D graphene network as binder-free anode for high performance lithium-ion batteries. Chem Eng J 313:1623–1632

Jiang TC, Bu FX, Feng XX, Shakir I, Hao GL, Xu YX (2017) Porous Fe_2O_3 nanoframeworks encapsulated within three-dimensional graphene as high-performance flexible anode for lithium-ion battery. ACS Nano 11:5140–5147

Kobayashi Y, Abe J, Kawase K, Takahashi K, Vogt BD, Shiratori S (2018) Enhanced stability of smoothly electrodeposited amorphous Fe_2O_3@electrospun carbon nanofibers as self-standing anodes for lithium ion batteries. New J Chem 42: 1867–1878

Li M, Lu J, Chen ZW, Amine K (2018) 30 years of lithium-ion batteries. Adv Mater 1800561

Liao KX, Chen ST, Wei HH, Fan JC, Xu QJ, Min YL (2018) Micropores of pure nanographite spheres for long cycle life and high-rate lithium-sulfur batteries. J Mater Chem A 6: 23062–23070

Lin LY, Li QB, Nie SY, Peng XH, Hu N (2016) 3D $ZnCo_2O_4$ nanowires@MnO_2 nanosheets core-shell structures grown on carbon cloth for excellent supercapacitor electrodes. Ceram Int 42:19343–19348

Luo DW, Lin F, Xiao WD, Zhu WD (2017) Synthesis and electrochemical performance of α-Fe_2O_3@carbon aerogel composite as an anode material for Li-ion batteries. Ceram Int 43: 2051–2056

Lv XX, Deng JJ, Wang BQ, Zhong J, Sham TK, Sun XH, Sun XL (2017) γ-Fe_2O_3@CNTs anode materials for lithium ion batteries investigated by electron energy loss spectroscopy. Chem Mater 29:3499–3506

Meng JK, Fu L, Liu YS, Zheng GP, Zheng XC, Guan XX, Zhang JM (2017) Gas-liquid interfacial assembly and electrochemical properties of 3D highly dispersed α-Fe_2O_3@graphene aerogel composites with a hierarchical structure for applications in anodes of lithium ion batteries. Electrochim Acta 224:40–48

Nie P, Shen L, Luo HF, Ding B, Xu GY, Wang J, Zhang XG (2014) Prussian blue analogues: a new class of anode materials for lithium ion batteries. J Mater Chem A 2:5852–5857

Pramudita JC, Schmid S, Godfrey T, Whittle T, Alam M, Hanley T, Brand HEA, Sharma N (2014) Sodium uptake in cell construction and subsequent in operando electrode behaviour of Prussian blue analogues, $Fe[Fe(CN)_6]_{1-x}{\cdot}yH_2O$ and $FeCo(CN)_6$. Phys Chem Chem Phys 16:24178–24187

Qiu WT, Balogun MS, Luo Y, Chen KQ, Zhu YK, Xiao XJ, Lu XH, Liu P, Tong YX (2016) Three-dimensional Fe_3O_4

nanotube array on carbon cloth prepared from a facile route for lithium ion batteries. Electrochim Acta 193:32–38

Shan XY, Zhang S, Zhang N, Chen YJ, Gao H, Zhang XT (2018) Synthesis and characterization of three-dimensional MoS_2@carbon fibers hierarchical architecture with high capacity and high mass loading for Li-ion batteries. J Colloid Interf Sci 510:327–333

Shao JX, Feng JH, Zhou H, Yuan AH (2019) Graphene aerogel encapsulated Fe-Co oxide nanocubes derived from Prussian blue analogue as integrated anode with enhanced Li-ion storage properties. Appl Surf Sci 471:745–752

Tjandra R, Li G, Wang XL, Yan J, Li M, Yu A (2016) Flexible high performance lithium ion battery electrode based on a free-standing TiO_2 nanocrystals/carbon cloth composite. RSC Adv 6:35479–35485

Wang XH, Zhang M, Liu EZ, He F, Shi CS, He CN, Li JJ, Zhao NQ (2016) Three-dimensional core-shell Fe_2O_3@carbon/carbon cloth as binder-free anode for the high-performance lithium-ion batteries. Appl Surf Sci 390:350–356

Wang XF, Tang YH, Shi PH, Fan JC, Xu QJ, Min YL (2018a) Self-evaporating from inside to outside to construct cobalt oxide nanoparticles-embedded nitrogen-doped porous carbon nanofibers for high-performance lithium ion batteries. Chem Eng J 334:1642–1649

Wang JP, Zhou H, Zhu MZ, Yuan AH, Shen XP (2018b) Metal-organic framework-derived Co_3O_4 covered by MoS_2 nanosheets for high-performance lithium-ion batteries. J Alloy Compd 744:220–227

Wei X, Li WH, Shi JA, Gu L, Yu Y (2015) FeS@C on carbon cloth as flexible electrode for both lithium and sodium storage. ACS Appl Mater Interfaces 7:27804–27809

Xie QX, Zhang YF, Zhu YT, Fu WG, Zhang X, Zhao P, Wu SH (2017) Graphene enhanced anchoring of nanosized Co_3O_4 particles on carbon fiber cloth as free-standing anode for lithium-ion batteries with superior cycling stability. Electrochim Acta 247:125–131

Xiong QQ, Tu JP, Xia XH, Zhao XY, Gu CD, Wang XL (2013) A three-dimensional hierarchical Fe_2O_3@NiO core/shell nanorod array on carbon cloth: a new class of anode for high-performance lithium-ion batteries. Nanoscale 5:7906–7912

Xu PP, Wang G, Yan JF, Zhang ZY, Xu MZ, Cai SB, Ruan XF, Deng ZH (2017) Reversible and high-capacity SnO_2/carbon cloth composite electrode materials prepared by magnetron sputtering for Li-ion batteries. Mater Lett 190:56–59

Zhang L, Wu HB, Madhavi S, Hng HH, Lou XW (2012) Formation of Fe_2O_3 microboxes with hierarchical shell structures from metal-organic frameworks and their lithium storage properties. J Am Chem Soc 134:17388–17391

Zhang GH, Hou SC, Zhang H, Zeng W, Yan FL, Li CC, Duan HG (2015) High-performance and ultra-stable lithium-ion batteries based on MOF-derived ZnO@ZnO quantum dots/C core-shell nanorod arrays on a carbon cloth anode. Adv Mater 27:2400–2405

Zhao SH, Guo JX, Jiang F, Su QM, Du GH (2016a) Porous $CoFe_2O_4$ nanowire arrays on carbon cloth as binder-free anodes for flexible lithium-ion batteries. Mater Res Bull 79:22–28

Zhao SH, Guo JX, Jiang F, Su QM, Zhang J, Du GH (2016b) Growth of hierarchal porous CoO nanowire arrays on carbon cloth as binder-free anodes for high-performance flexible lithium-ion batteries. J Alloy Compd 65:372–377

Zheng ZM, Zao Y, Zhang QB, Cheng Y, Chen HX, Zhang KL, Wang MS, Peng DL (2018) Robust erythrocyte-like Fe_2O_3@carbon with yolk-shell structures as high-performance anode for lithium ion batteries. Chem Eng J 347:563–573

Zhu JX, Yin ZY, Yang D, Sun T, Yu H, Hoster HE, Hng HH, Zhang H, Yan QY (2013) Hierarchical hollow spheres composed of ultrathin Fe_2O_3 nanosheets for lithium storage and photocatalytic water oxidation. Energy Environ Sci 6:987

Zhu XM, Jiang XY, Chen X, Liu XL, Xiao LF, Cao YL (2017) Fe_2O_3 amorphous nanoparticles/graphene composite as high-performance anode materials for lithium-ion batteries. J Alloy Compd 711:15–21

Zhu MZ, Zhou H, Shao JX, Feng JH, Yuan AH (2018) Prussian blue nanocubes supported on graphene foam as superior binder-free anode of lithium-ion batteries. J Alloy Compd 749:811–817